Journal of Molecular Liquids 401 (2024) 124537

Contents lists available at ScienceDirect

Journal of Molecular Liquids

journal homepage: www.elsevier.com/locate/molliq

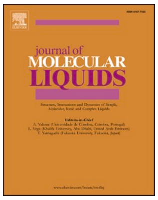

Ultra-high dilutions analysis: Exploring the effects of potentization by electron microscopy, Raman spectroscopy and deep learning

Camelia Berghian-Grosan [a], Sahin Isik [b], Alin Sebastian Porav [a], Ilknur Dag [c,d], Kursad Osman Ay [c], George Vithoulkas [e]

[a] National Institute for Research and Development of Isotopic and Molecular Technologies, Cluj-Napoca 400293, Romania
[b] Computer Engineering Department, Eskisehir Osmangazi University, Eskisehir 26480, Turkey
[c] Central Research Laboratory Application and Research Center, Eskisehir Osmangazi University, Eskisehir 26480, Turkey
[d] Vocational Health Services High School, Eskisehir Osmangazi University, Eskisehir 26480, Turkey
[e] University of the Aegean, Mytilene 81100, Greece

ARTICLE INFO

Keywords:
Aurum metallicum
Ultra-high dilutions
Potentization
Cluster assemblies
Artificial intelligence
Raman data

ABSTRACT

The subject of ultrahigh dilutions has been under continuous debate over the years, mainly because the possibilities to analyze such diluted solutions are limited. In this context, transmission electron microscopy (TEM) investigations were conducted to evaluate the morphological characteristics of ethanol- and water-based highly diluted solutions of gold; three levels of potentization (6C, 30C, and 200C) were examined for each type of solution. Moreover, Raman spectroscopy and deep learning (DL) algorithms were employed for the analysis of the three potentization levels of purified water, unpurified water, and purified water-based gold solutions. Three batches were assessed for each considered category, and the ability to discriminate between all investigated classes, between the potencies within each group or between the classes within the same level of potentization were presented and discussed in correlation with the TEM findings. Distinct forms of organization were revealed by TEM for the three levels of potentization, while the gated recurrent unit (GRU) model showed great accuracy (88 %) for discriminating all classes, over 90 % accuracy for distinguishing the samples within each group and over 95 % accuracy for classification within the same level of potentization if unpretreated Raman spectra were used. Thus, this suite of methods (TEM-EDX and Raman spectroscopy in combination with DL) can be successfully used for the characterization and differentiation of highly diluted solutions resulting after potentization treatment. Furthermore, considering the results obtained from the discrimination study involving all 11 classes and a data augmentation approach, the spectral segmentation method can be seen as a valuable strategy for increasing the model prediction accuracy.

1. Introduction

Potentization is a process that involves successive dilutions and succussions (vigorous shaking); it was first introduced by the German physician Samuel Hahnemann, who observed that solutions of substances that have undergone this process have a biological effect in humans - with therapeutic evidence [1]. To date, numerous homeopathic remedies have been used, and they are very well documented [2–6]; they are derived from a wide variety of substances that undergo potentization to obtain their healing properties. Several insightful perspectives have attempted to explain the action of homeopathic remedies [7–11]. The impact of succussion (vigorously shaking) on some pharmaceutical preparations, such as Echinacea 10^{-2}, Baptisia 10^{-3}, Baptisia 10^{-4}, Luffa 10^{-4}, and Spongia 10^{-6}, was recently highlighted via the aid of droplet evaporation and statistical analysis; the samples were manufactured in accordance with the European Pharmacopoeia rules for homeopathic drugs, and the authors employed 0, 10, or 100 succussion strokes. The results showed significant differences for all the investigated preparations [12]. Moreover, the effects of mechanical shocks (i.e., agitation, dropping) on protein solutions are well known, and measures for mitigating these effects have been investigated and proposed in some studies [13,14]. However, for homeopathy, shaking together with dilution is an essential tool for remedy preparation.

A major concern regarding potentized solutions at high dilutions (30C, 200C, etc.) beyond the Avogadro number, which sets the dilution limit (12C) beyond which the original substance cannot be present, is

---

E-mail addresses: camelia.grosan@itim-cj.ro (C. Berghian-Grosan), george@vithoulkas.com (G. Vithoulkas).

https://doi.org/10.1016/j.molliq.2024.124537
Received 22 January 2024; Received in revised form 17 March 2024; Accepted 20 March 2024

that the starting material is not expected to be found in even the slightest amount [15]. Nevertheless, in a study based on medicines obtained from metals, Chikramane et al. [10] demonstrated the presence of the starting materials, in the form of nanoparticles, in extreme dilutions of 30C and 200C by transmission electron microscopy (TEM), electron diffraction and inductively coupled plasma–atomic emission spectroscopy (ICP–AES). Various techniques have been used over the years for the characterization of homeopathically prepared remedies, highlighting the existence of specific structures even in highly diluted medicines [16–24]. However, within the scientific community, it is well known that the Benveniste experiment [25], shortly after the release of its findings, was proven false by a scientific committee sent by the journal Nature to the author's laboratory, as explained by George Vithoulkas in his paper, "The controversy over the memory of the water" [26].

Water is a special solvent that plays an important role in biological and chemical processes [27]. Therefore, understanding the anomalous properties of liquid water has been of continuous interest, and many experimental and theoretical studies have been carried out to understand its structure [28,29]. Nevertheless, the structure and dynamics of water are still under continuous debate [30]. The sensitivity of the OH stretching mode to different local environments allows the use of vibrational spectroscopy in the study of the structure and dynamics of liquid water [28]. The investigation of liquid water by infrared and Raman spectroscopy reveals broad peaks in the OH stretching region, suggesting multiple underlying contributions (from various species induced by different local hydrogen-bonding arrangements), while distinct peaks can be clearly seen in the spectra of ice [31]. In 2009, Sun [32] analyzed liquid water under ambient conditions by Raman spectroscopy and proposed the deconvolution of the OH stretching region into five subbands. However, due to the complexity of water and the high dilutions of the investigated solutions, such analysis is a very difficult task. To address these difficulties, chemometric techniques and, more recently, machine learning (ML) models have been applied to Raman signals for analysis and data learning [33].

ML algorithms are currently gaining increasing popularity in classification applications [34,35]. Recently, traditional and deep learning algorithms methods have successfully been applied to discriminate the Raman spectra of various complex materials (i.e., minerals) or classify high-dimensional spectroscopic data [36–38].

Deep learning (DL) is a subfield of ML that is substantially more robust than feature engineering-based methods that were used in the past. DL approaches have many benefits, including being time-efficient, requiring no feature construction, and yielding superior outcomes. Artificial neural networks, often known as ANNs, are the precursors of DL techniques. ANNs consist of an input layer, one or more middle levels (layers), and an output layer. These approaches are often trained by supervised learning, which means that predefined labels are used for a set of data in the training process. The convolutional neural network (CNN) [39], one of the most representative DL networks, is a type of forward feedback neural network that uses convolutional operations and a very large number of filters. There are many different types of convolutional-based learning algorithms that can be used according to the desired task. Typically, 2-D CNN models are utilized for image-driven applications. The gated recurrent unit (GRU) [40,41] and 1-D CNN models are utilized to handle time series-based prediction or classification tasks. The key motivation is that recurrent models have the potential ability to preserve long-term relationships between sequence data. These approaches provide a substantial amount of assistance in resolving the vanishing gradient problem [42].

The present work investigates the structural organization of potentized ethanol- and water-based solutions of gold, a homeopathic remedy named Aurum metallicum (AUR). Three highly diluted (6C, 30C and 200C) AUR solutions were subjected to TEM analysis by two independent laboratories located in Romania and Turkey. Different organizations of these solutions were confirmed by both labs. The choice of these centesimal dilutions was motivated by the need to investigate solutions containing low amounts of the initial substance, even beyond the Avogadro number (i.e., the latter two dilutions investigated). Raman spectra were also obtained for various potentized water-based solutions (purified water (PW), unpurified water (UW) and PW-based gold solution (AUR)) and processed by DL algorithms to investigate the ability of the GRU models to discriminate between all these solutions and classify the samples within the investigated categories (AUR, PW, and UW) or within the three levels of potentization (6C, 30C, and 200C). DL was utilized to evaluate its efficiency for Raman spectra classification. Raman spectral values are assumed to be time series values; hence, we applied a recurrent neural network. We performed experiments with the GRU model since it solves both the vanishing gradient problem and the speed issue. Thus, we tested the capacity of this classification approach to be used, in combination with Raman spectroscopy, for the analysis of water-based solutions obtained after potentization. Our results allowed us to prove that this suite of methods (TEM-EDX and Raman spectroscopy in combination with DL) can be successfully used for the characterization and differentiation of highly diluted solutions resulting after the potentization treatment.

2. Material and methods

2.1. Materials

All the investigated solutions were prepared by the Korres company (Athens, Greece), a company certified by the National Medicines Agency (EOF - Greece). These solutions were produced in accordance with the German Homeopathic Pharmacopoeia (GHP), adhering to Good Manufacturing Practice (GMP) guidelines [43], and taking European Pharmacopoeia procedures for conformity tests into account, with a few clearly indicated exceptions. Specifically, the exceptions pertain to the solvents used in the final step of the preparation process: 50 % v/v ethanol for ethanol-based solutions and purified water for water-based solutions. The solutions were categorized, based on the starting material, into three groups: purified water (PW), unpurified water (UW), and Aurum metallicum (AUR). For each category, three potency levels (6C, 30C, and 200C) were prepared, with three batches of each potency level produced on different days. The C notation is associated with centesimal dilution and means 1 part of the concentrated solution/previously potentized solution to 99 parts of eluent (mass/mass).

For the PW and UW samples, the objective was to prepare potentized solutions that are analogous to medicinal solutions in all respects except for the absence of an active medicinal ingredient. PW (conformity according to the European Pharmacopoeia – Ph. Eur.) is generally used for the preparation of homeopathic remedies, while UW is partially purified. The water types employed in this study had the following characteristics, as indicated by the Korres company: PW – conductivity 0.7–0.88 μS/cm, pH 6.4–6.8, NO_3^- <0.2 ppm, and metal ions, Al < 3–5 ppb, As < 0.005 ppm, Pb 0.00032 ppm, Cd < 0.001 ppm, Hg < 0.0005 ppm (total heavy metals 0.00682 ppm, limit < 0.1 ppm); UW - conductivity 196 μS/cm, pH 7.8, HCO_3^- 66 ppm, Cl^- 22 ppm, NO_3^- 9.8 ppm, Na^+ 15 ppm, Ca^{2+} 10 ppm, Mg^{2+} 8.8 ppm, CO_2 9.7 ppm. Thus, the Ph. Eur. purified water and unpurified water, respectively, were used as starting material. The Ph. Eur. purified water was also employed in the dilution process and, due to the specific experimental purposes, in the preparation processes of the 30C and 200C PW and UW solutions.

For AUR category, a method based on the trituration of Aurum metallicum with lactose monohydrate, as the vehicle, was firstly involved up to 4C level; then, in order to obtain 6C liquid potency, the protocol employed purified water (conformity according to the Ph. Eur.) for the preparation of 5C potency and ethanol 30 % (m/m) for 6C liquid dilution manufacturing. Starting from 6C and up to 29C, and accordingly up to C199, the Ph. Eur. purified water was used in the preparation process. The final potentized solutions of 30C and 200C were produced with ethanol 50 % (v/v) for ethanol-based AUR solutions. Due to the specific experimental purposes, the Ph. Eur. purified water was used in the preparation processes of the 30C and 200C water-based AUR solutions.

2.1.1. *Transmission electron microscopy*

For the TEM studies, two types of AUR samples were involved; the first type, AUR prepared in 50 % v/v ethanol solution, was analyzed in Romania and denoted E-AUR, while the second type of AUR was prepared only in purified water (PW) and was subjected to analysis in Turkey (denoted W-AUR). For both types of AUR, three potentized samples were investigated, namely, 6C, 30C and 200C.

2.1.2. *Raman investigations*

For the Raman investigations, three types of solutions were used: purified water (PW), unpurified water (UW) and AUR. Additionally, for the PW and UW groups, we considered nonpotentized samples (reference samples of the water types used for the potentization process) and three types of potentized water samples (6C, 30C and 200C); for each type of potentized water samples, three batches were prepared on three different days. For the AUR category, only the water-based potentized solutions were investigated. This means a total of 12 samples for PW, 12 samples for UW, and 9 samples for AUR were considered.

2.2. *Methods*

2.2.1. *Romanian TEM and EDX procedures*

Structural and morphological characterization of the AUR samples was realized on a Hitachi HD-2700 scanning transmission electron microscope (STEM) equipped with a secondary electron (SE) detector, a transmitted electron (TE) detector (Hitachi High Tech., Japan) and a cold field emission gun designed for high-resolution (HRTEM) imaging with a resolution of 0.144 nm. Carbon-coated TEM grids were treated with 6 μl of the potentized solutions of AUR, which were previously succussed 10 times for homogenization. After 1–2 min, the excess liquid was blotted by Whatman grade 1 filter paper, and the grids were allowed to dry in air. The samples were analyzed using the STEM system operated at 200 kV. A dual EDX system consisting of an X-Max N100TLE silicon drift detector (SDD) (Oxford Instruments) was used for the EDX investigations.

2.2.2. *Turkish TEM and EDX procedures*

TEM images of the three potencies (6C, 30C and 200C) of AUR were obtained using a Hitachi HT 7800 TEM operating at an acceleration voltage of 100 kV. After each sample was shaken 10 times, 1 drop was dripped onto a carbon-coated grid and allowed to dry in a clean environment. EDX analysis of samples was performed using an Oxford Instruments X-MaxN connected to the same TEM device to confirm the presence of gold.

The histograms prepared for both the Romanian and Turkish TEM images were realized based on data obtained with ImageJ software (NIH, USA).

2.2.3. *Raman spectroscopy*

Raman spectra were recorded on an NRS-3300 Raman spectrometer (Jasco, Japan) equipped with a charge-coupled device (CCD) detector using 514.5 nm laser (green light) excitation. The solutions were analyzed in glass capillary tubes (Marienfeld, Germany) with a diameter of 1.5–1.6 mm. An Olympus UMPLFL 20X objective, 600 l/mm grating, 0.1 × 6 mm slit, exposure time of 120 s and three scans were employed to record the Raman spectra from approximately 72 cm^{-1} to 4020 cm^{-1}. The 521 cm^{-1} peak, corresponding to Si, was used to calibrate the spectrometer. Raw and noisy data were not denoised or smoothed out, and outliers were not removed from the dataset. The preprocessing of data involved two main steps and was realized with Spectra Manager (JASCO) and OriginPro 2023 (OriginLab Corporation). The first data pretreatment step selected a wavenumber interval of 180 to 4000 cm^{-1} and limited the number of features to below 13,000 by applying a 3rd-order spline method with a data pitch of 0.3. These data were further normalized to [0,1] and considered for DL investigation as unpretreated Raman data. The second step involved a baseline subtraction (bg) process that was applied in OriginPro to the data obtained, before normalization, from the first step. In order to apply the bg process, the following steps were performed: user-defined baseline mode, the 2nd derivative (zeroes) method for anchor point detection, snap to spectrum, the line interpolation method and the same number of baseline points as input data [44]. The as-obtained data were further normalized to [0,1] before their use in constructing the bg-pretreated datasets for the DL study.

2.2.4. *Deep learning*

DL investigations were carried out using the Python programming language and Colab Pro, which provides an accelerated computing environment. The GRU model was built and trained using the Keras 2.12.0 library. The Colab Tesla T4 GPU was utilized for training the model with a large batch size. The Tesla T4 has a total of 2560 CUDA cores, as well as computing 3.7, 15 GB of memory, and GDDR6 VRAM. Additionally, the Sklearn 1.2.2 package was utilized to analyze and explain the obtained findings. More details regarding the protocol for DL investigations are presented in Supplementary Material file and Figs S1 and S2.

3. Results

To determine the ability of our proposed method for the characterization of various solutions and potencies, we first aimed to determine the properties of the samples by TEM analysis.

3.1. *TEM investigation*

TEM is a valuable tool that provides fundamental data about the organization of nanomaterials; this knowledge is very important for understanding and development in materials science, as well as for fields using highly diluted solutions that are also composed of nanostructures.

3.1.1. *Aurum metallicum 6C*

Fig. 1 presents several TEM images obtained with two different instruments (see Methods section) for the 6C potency of AUR. Two different media were employed for sample preparation – the first medium was a 50 % v/v ethanol solution, which was used for the AUR samples analyzed in Romania (E-AUR 6C). The second medium was purified water, which was employed for the samples investigated in Turkey (W-AUR 6C).

Despite the underlying differences in solvents, the obtained TEM images are quite similar regarding the shape of the nanoparticles. However, the nanoparticle size depends on the solvent type. This is revealed in the histograms of the two samples, indicating smaller nanoparticles for E-AUR 6C than for W-AUR 6C (Fig. 1C and G), most likely because ethanol is more effective as a stabilizing agent than water. The EDX data (insets of Fig. 1 and Figs. S3 and S4) show comparable percentages of gold (Au) in both samples and the presence of silicon (Si) and oxygen (O) (the copper (Cu) is from the grid).

3.1.2. *Aurum metallicum 30C*

Furthermore, the 30C potency of AUR was investigated; Fig. 2 and Figs. S5-S8 show the TEM images, EDX data and TEM-EDX mapping results for this potency. Here, it is worth mentioning the similarities between the two samples, E-AUR 30C and W-AUR 30C, in terms of the nanostructure shape and the appearance of impurities.

As in the previous case, potency 6C, the size of the nanoparticles/nanostructures of 30C potency tends to be smaller for E-AUR than W-AUR (Fig. 2C and G); this behavior is explained by the capacity of ethanol to act as an efficient stabilizing agent. Moreover, the histograms in Figs. 1 and 2 indicate smaller nanostructures in E-AUR 30C than E-

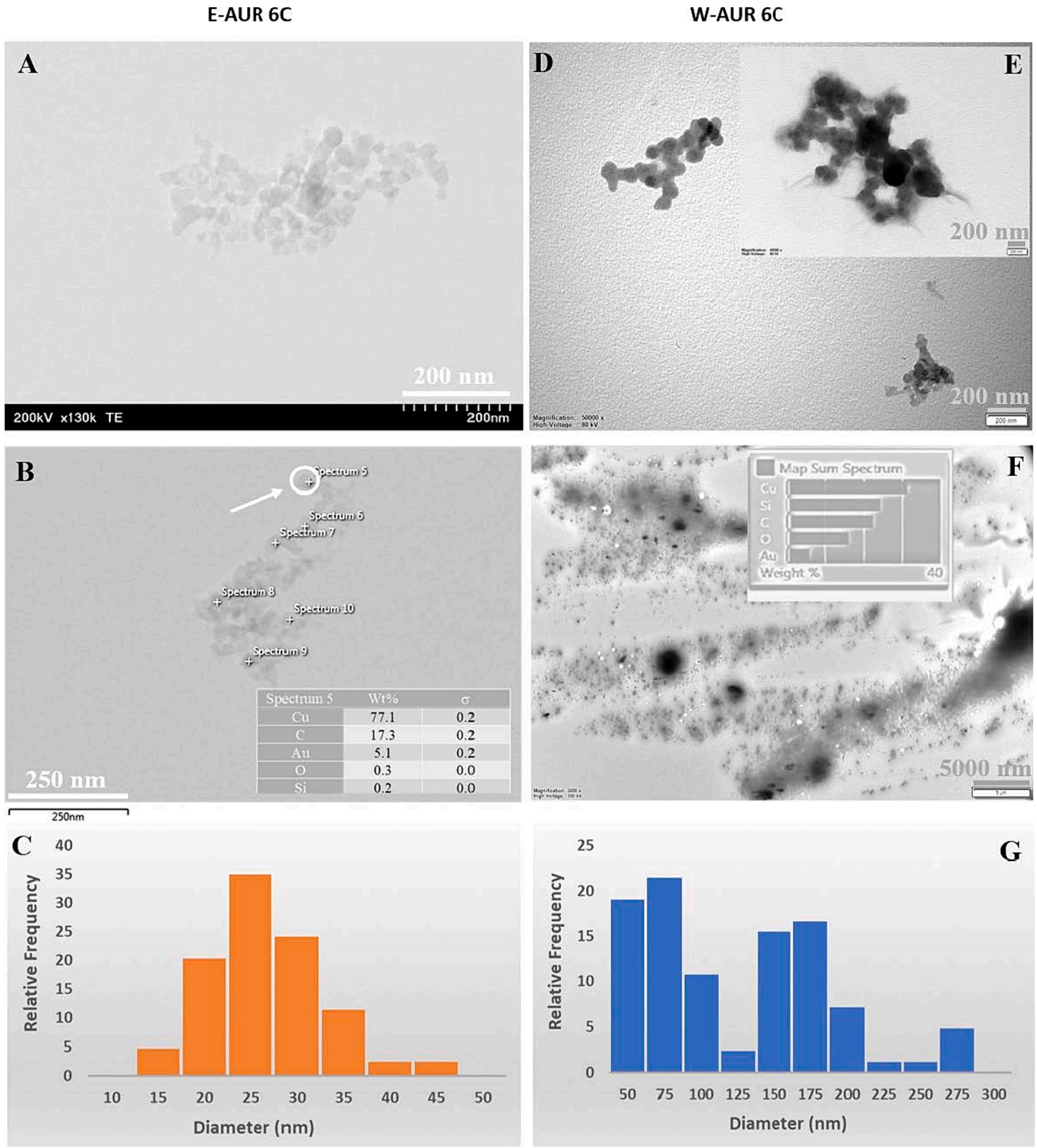

Spectrum 5	Wt%	σ
Cu	77.1	0.2
C	17.3	0.2
Au	5.1	0.2
O	0.3	0.0
Si	0.2	0.0

Fig. 1. TEM data for the 6C potency of AUR. (A-C) TEM images and histogram of the relative frequency of nanoparticle sizes for the AUR ethanol-based samples and (D-G) for the water-based samples; inset – EDX data for the marked points or the sum spectrum.

AUR 6C and a significant decrease in size of more than 150 nm relative to the water-based samples; these large structures are clearly seen in W-AUR 6C, but they are visible only in traces in the W-AUR 30C sample. This significant change between the profiles of the two potencies, 6C and 30C, appears after the potentization process, which involves several successive dilutions and successions.

3.1.3. *Aurum metallicum 200C*

The characteristics of the 200C potency are illustrated in Fig. 3 and Figs. S9-S11 and were obtained by analyzing two samples (E-AUR 200C – prepared using aqueous 50 % v/v ethanol solution and W-AUR 200C – obtained only with purified water).

The general tendency observed for the 6C and 30C potencies is also present here; more precisely, the size of the nanostructures in the E-AUR 200C sample is smaller than those in W-AUR 200C, as revealed in the histograms in Fig. 3. Moreover, for both 200C samples, the nanoparticles are larger than the nanoparticles observed at 30C potency and are very different in size and shape from the nanoparticles at 6C potency (Figs. 1-3).

Distinct organization and a total lack of impurities inside some AUR 200C cluster assemblies are evident in Fig. 3B. Moreover, both AUR 200C samples display a preferential branched assembly mode (Fig. 3A and D), and the presence of small amounts of impurities such as Si and Fe in these clusters is demonstrated by the EDX data presented in the inset of Fig. 3 and Figs. S9 and S11B.

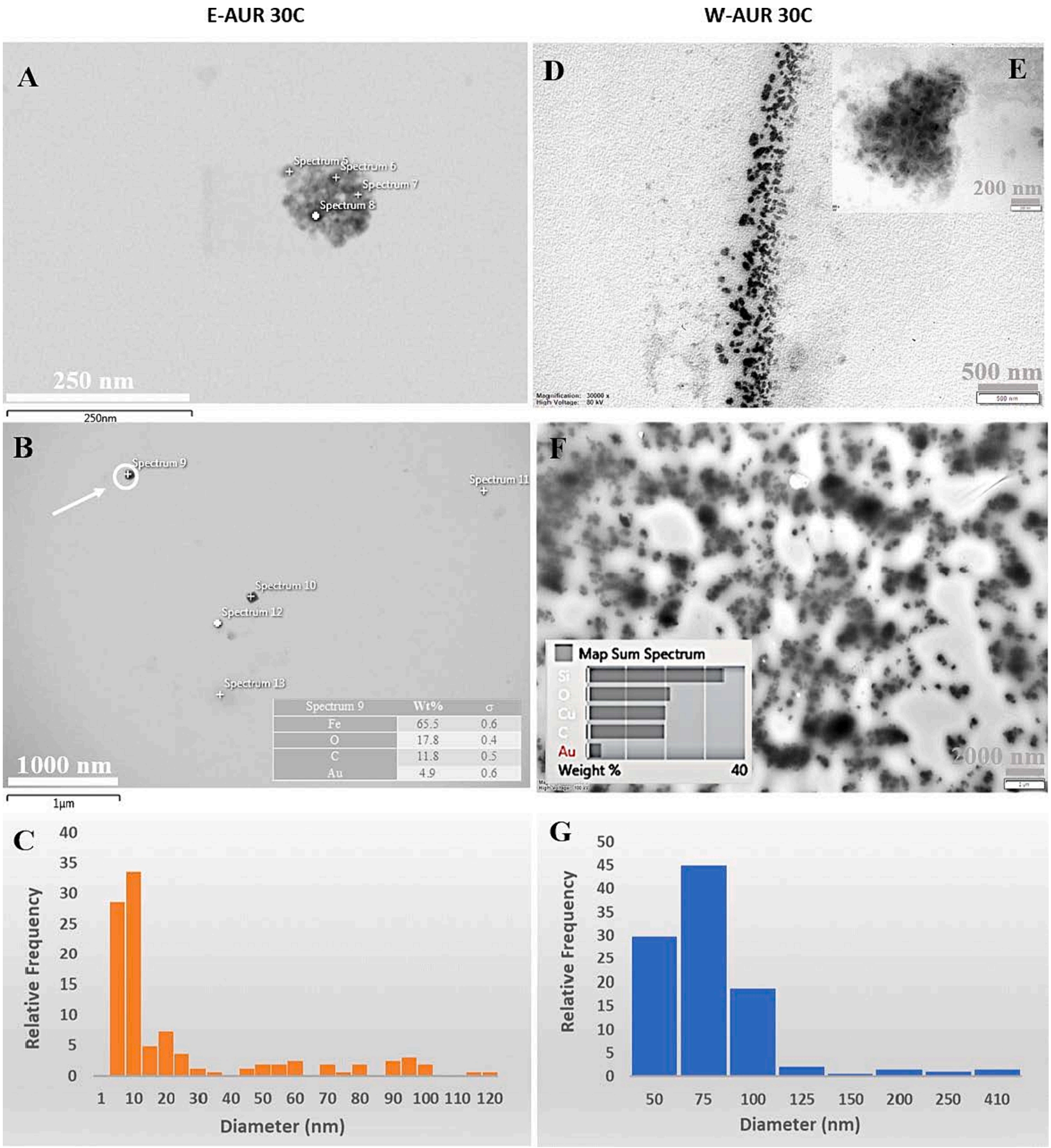

Spectrum 9	Wt%	σ
Fe	65.5	0.6
O	17.8	0.4
C	11.8	0.5
Au	4.9	0.6

Fig. 2. TEM data for the 30C potency of AUR. (A-C) TEM images and histogram of the relative frequency of nanoparticle sizes for the AUR ethanol-based samples and (D-G) for the water-based samples; inset – EDX data for the marked points or the sum spectrum.

3.2. Raman spectroscopy and deep learning investigations

After conducting the TEM studies, a rapid and nondestructive technique such as Raman spectroscopy can be considered for the analysis of the investigated solutions. Due to the larger assemblies observed in TEM for the water-based samples and considering the Raman peculiarities of water–ethanol solutions, Raman spectroscopy was applied to the water-based solutions only. The objective was to investigate the transformations that appear in three groups/categories: PW, UW, and AUR. PW is generally employed for homeopathic remedy preparation, while UW is a partially purified form of water; these types of water possess different characteristics. Here, we note the low conductivity of the PW samples (0.7–0.88 μS/cm) and their low levels of ions (NO_3^- <0.2 ppm, Al $<$ 3–5 ppb, total heavy metals 0.00682 ppm); moreover, the UW samples have higher conductivity (196 μS/cm) as well as higher concentrations of different ions (nitrate, bicarbonate, sodium, etc.). See the Material and Methods section for more details.

Potentization was applied to PW, UW, and AUR samples prepared on three different days to obtain three batches of potentized samples at 6C, 30C and 200C potencies. PW and UW are not generally potentized for commercialization; the potentization procedure was applied to them only for this study. Thus, 33 samples were analyzed by Raman spectroscopy. Each sample was analyzed at 5 points to obtain representative data of the investigated solutions. A total of 165 Raman spectra (range 180–4000 cm^{-1}) were subjected to the classification study. The raw and bg-pretreated Raman spectra obtained during this experiment, for different levels of potentization (6C, 30C, and 200C) of the investigated sample types (PW, UW and AUR), are shown in Figs. S12-S17.

3.2.1. Classifying all classes with deep learning by using the GRU model

The Raman spectral classification results for the 11 different classes obtained using the trained GRU model are displayed in Fig. 4; both unpretreated and bg-pretreated sets of data were considered.

The confusion matrix is displayed to provide a summary of the

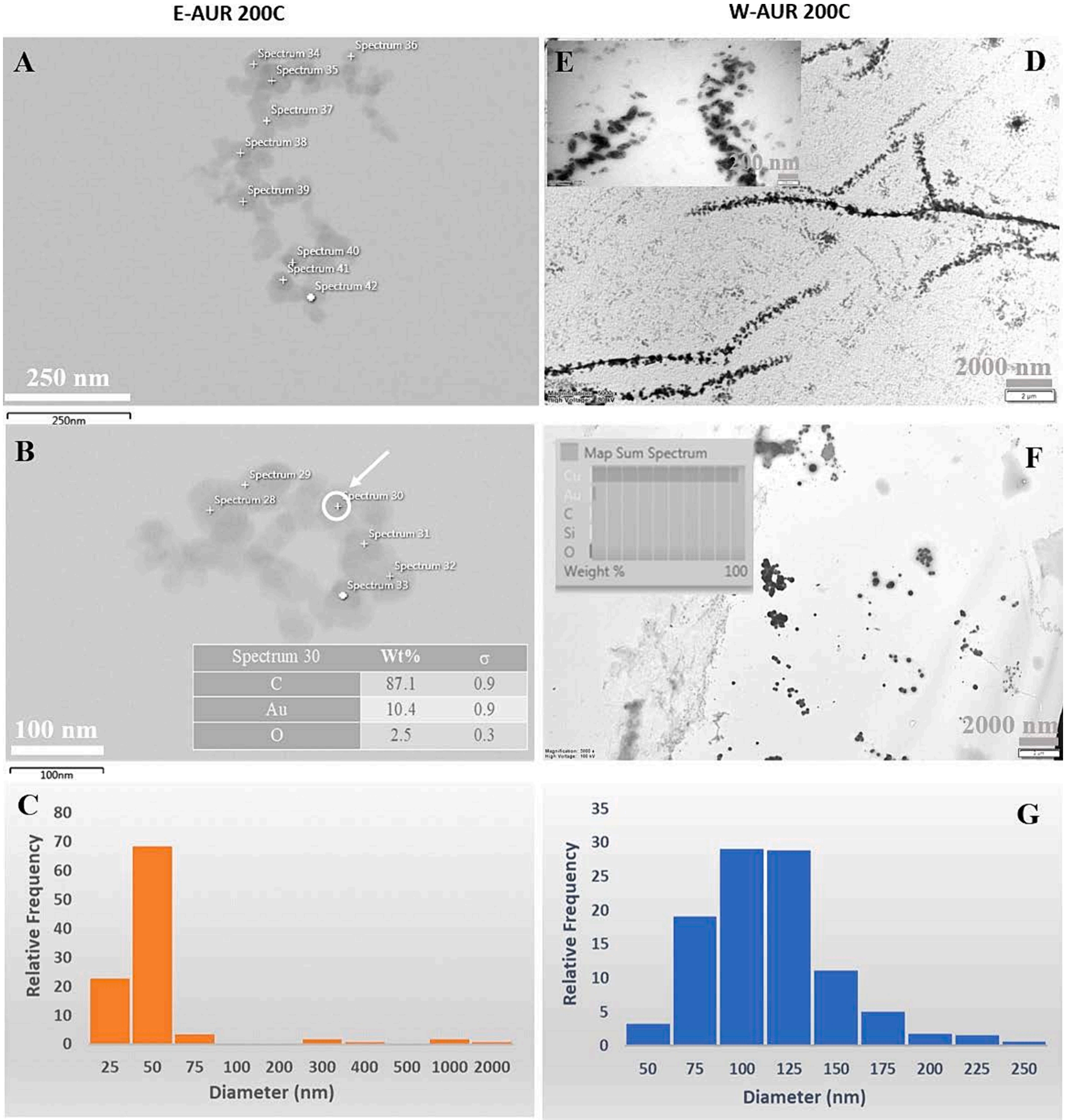

Spectrum 30	Wt%	σ
C	87.1	0.9
Au	10.4	0.9
O	2.5	0.3

Fig. 3. TEM data for the 200C potency of AUR. (A-C) TEM images and histogram of the relative frequency of nanoparticle sizes for the ethanol-based samples and (D-G) for the water-based samples; inset – EDX data for the marked points or the sum spectrum.

number of instances in which the GRU model accurately or erroneously predicted the outcome. The model demonstrates a very good recognition capacity in comparing the three investigated categories; thus, it shows great efficiency in discriminating between the AUR, PW and UW categories when unpretreated Raman data are considered (Fig. 4A). In this case, an accuracy of 88 % (Table 1) can be noted; this value can be regarded as very good, especially if the great similarities between the investigated classes are considered. This value, which is a little less than 90 %, represents mostly the result of wrong assignments generated for different potentization levels or reference samples belonging to the same category; only 3 wrong assignments have been registered between the three investigated classes - AUR, PW, UW (one sample of AUR200C was associated to UW200C and two samples of UW30C were allocated to AUR6C and AUR200C, respectively).

Thus, for the AUR category, the other three wrong assignments were due to the similarities between different levels of potentization within the group. A similar behavior has been also observed within the PW and UW groups. There were no errors related to the differentiation of PW from AUR or UW samples. Within the PW and UW groups, correct recognition was observed for the 200C potency level, while for the other levels of potentization, up to 5 samples were wrongly assigned (this maximum was reached in the PW6C class).

However, when the GRU model was applied to the bg-pretreated dataset, the results showed an accuracy of only 59 % (Fig. 4B and Table 1). Major incorrect classification results were obtained within the three investigated groups, but there were also some wrong assignments to samples outside the proper group. These results show that the poor recognition capacity of the model is due to the loss of information that occurred when background subtraction was applied to the Raman data. The AUR and UW groups seem to be the most affected (Fig. 4B).

Table 1 presents an in-depth analysis of the performance values of the proposed approach. The precision, recall, and f1 values for each class were determined independently. The results of the experiments indicated that the macro f1 scores for the two datasets were 0.88 and 0.59. Notably, the PW, PW6C, PW30C, and PW200C categories have stable recognition rates across both datasets. When recall values are taken into account, the model has a tendency to underestimate the classification accuracy of UW30C samples. It can be deduced from the findings that overall, the discriminative power of this model for the UW data is somewhat limited. Furthermore, this work investigates the use of a well-known machine learning approach, specifically support vector machines (SVM), for the categorization of Raman data. Compared with the deep

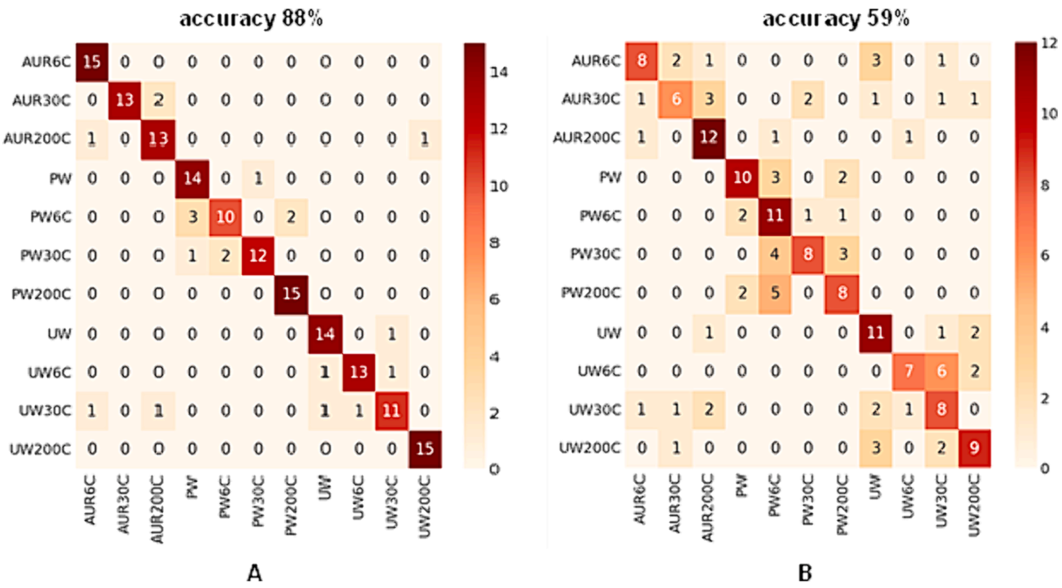

A

	AUR6C	AUR30C	AUR200C	PW	PW6C	PW30C	PW200C	UW	UW6C	UW30C	UW200C
AUR6C	15	0	0	0	0	0	0	0	0	0	0
AUR30C	0	13	2	0	0	0	0	0	0	0	0
AUR200C	1	0	13	0	0	0	0	0	0	0	1
PW	0	0	0	14	0	1	0	0	0	0	0
PW6C	0	0	0	3	10	0	2	0	0	0	0
PW30C	0	0	0	1	2	12	0	0	0	0	0
PW200C	0	0	0	0	0	0	15	0	0	0	0
UW	0	0	0	0	0	0	0	14	0	1	0
UW6C	0	0	0	0	0	0	0	1	13	1	0
UW30C	1	0	1	0	0	0	0	1	1	11	0
UW200C	0	0	0	0	0	0	0	0	0	0	15

B

	AUR6C	AUR30C	AUR200C	PW	PW6C	PW30C	PW200C	UW	UW6C	UW30C	UW200C
AUR6C	8	2	1	0	0	0	0	3	0	1	0
AUR30C	1	6	3	0	0	2	0	1	0	1	1
AUR200C	1	0	12	0	1	0	0	0	1	0	0
PW	0	0	0	10	3	0	2	0	0	0	0
PW6C	0	0	0	2	11	1	1	0	0	0	0
PW30C	0	0	0	0	4	8	3	0	0	0	0
PW200C	0	0	0	2	5	0	8	0	0	0	0
UW	0	0	1	0	0	0	0	11	0	1	2
UW6C	0	0	0	0	0	0	0	0	7	6	2
UW30C	1	1	2	0	0	0	0	2	1	8	0
UW200C	0	1	0	0	0	0	0	3	0	2	9

Fig. 4. Confusion matrix of the GRU model for (A) unpretreated and (B) bg-pretreated data of all investigated categories.

Table 1
Classification results obtained with unpretreated and baseline-subtracted (bg-pretreated) Raman data.

	GRU						**SVM**					
	unpretreated			**bg-pretreated**			**unpretreated**			**bg-pretreated**		
	prec	re	f1	prec	re	f1	prec	re	f1	prec	re	f1
AUR200C	0.88	1.00	0.94	0.73	0.53	0.62	0.64	0.60	0.62	0.35	0.40	0.38
AUR30C	1.00	0.87	0.93	0.60	0.40	0.48	0.52	0.73	0.61	0.10	0.13	0.11
AUR6C	0.81	0.87	0.84	0.63	0.80	0.71	0.36	0.33	0.34	0.17	0.20	0.18
PW	0.78	0.93	0.85	0.71	0.67	0.69	0.75	0.80	0.77	0.55	0.80	0.65
PW200C	0.83	0.67	0.74	0.46	0.73	0.56	0.53	0.53	0.53	0.50	0.53	0.52
PW30C	0.92	0.80	0.86	0.73	0.53	0.62	0.65	0.73	0.69	0.50	0.40	0.44
PW6C	0.88	1.00	0.94	0.57	0.53	0.55	0.64	0.47	0.54	0.17	0.13	0.15
UW	0.88	0.93	0.90	0.55	0.73	0.63	0.69	0.73	0.71	0.18	0.13	0.15
UW200C	0.93	0.87	0.90	0.78	0.47	0.58	0.64	0.60	0.62	0.58	0.47	0.52
UW30C	0.85	0.73	0.79	0.42	0.53	0.47	0.50	0.40	0.44	0.29	0.27	0.28
UW6C	0.94	1.00	0.97	0.64	0.60	0.62	0.80	0.80	0.80	0.55	0.40	0.46
macro avg	0.88	0.88	0.88	0.62	0.59	0.59	0.61	0.61	0.61	0.36	0.35	0.35
	Accuracy: 88 %			**Accuracy: 59 %**			**Accuracy: 61 %**			**Accuracy: 35 %**		

learning method (GRU), the traditional machine learning technique (SVM) yielded the lowest accuracy scores for the two datasets.

Considering these results, a more in-depth investigation was conducted, namely an intelligent data augmentation approach was employed to increase the dataset's size. Thus, by using a spectral segmentation strategy, every Raman spectrum was divided into smaller segments. The dimensions of the segment were found to be 1 × 1024. For example, when the sample size is decided to be 1 × 12733, a total of around 12 unique segments are acquired. The original dataset contains 15 instances for a certain class. Upon completion of the segmentation procedure, the dataset is resized to 1980 × 1024 and consists of 11 distinct classes. Thus, the size of samples per class becomes 180. The dataset is then partitioned, with 80 % allocated for training and the remaining portion reserved for testing purposes. The five-fold cross-validation was applied to measure the performance of our GRU model on obtained segmentation datasets. Following this approach, it was found that there is a direct relationship between increasing the size of the segment and the decrease in performance. The experimental results presented in Fig. S18 and Table S1, obtained by involving the samples from the testing sets, demonstrate that our GRU model achieves a high accuracy score of 99.45 % for unpretreated data and a perfect accuracy score of 100 % for bg-pretreated data across 11 classes. Even if further investigations, i.e. involving a larger number of samples, have to be made before proposing the spectral segmentation strategy as the most appropriate for experiments containing a high number of classes, this strategy can be considered as a valuable data augmentation approach for our type of data.

3.2.2. Classifying potencies within each group with deep learning by using the GRU model

The recognition rate obtained with the DL method within each category, (AUR 6C, AUR 30C, AUR 200C, PW), (PW, PW 6C, PW 30C, PW 200C) and (UW, UW 6C, UW 30C, UW 200C), was analyzed by involving unpretreated and bg-pretreated Raman data and the results were compared in terms of performance values. Fig. 5 illustrates the findings of the experiments after applying stratified 15-fold cross-validation (CV).

To allocate samples for validation and training purposes, we employed a 15-fold splitting technique, wherein 11 samples are selected for validation and the remaining samples are designated for training. For the AUR group, the nonpotentized PW class was used as a reference.

In the case of AUR vs. PW, the produced confusion matrices demonstrate that 98 % and 78 % accuracies were obtained, Fig. 5A,D. The findings showed accuracies of 90 and 75 % for the PW group, Fig. 5B,E, while accuracy values of 92 % and 68 % were obtained for the UW group, Fig. 5C,F. In general, the PW6C and UW30C groups have low

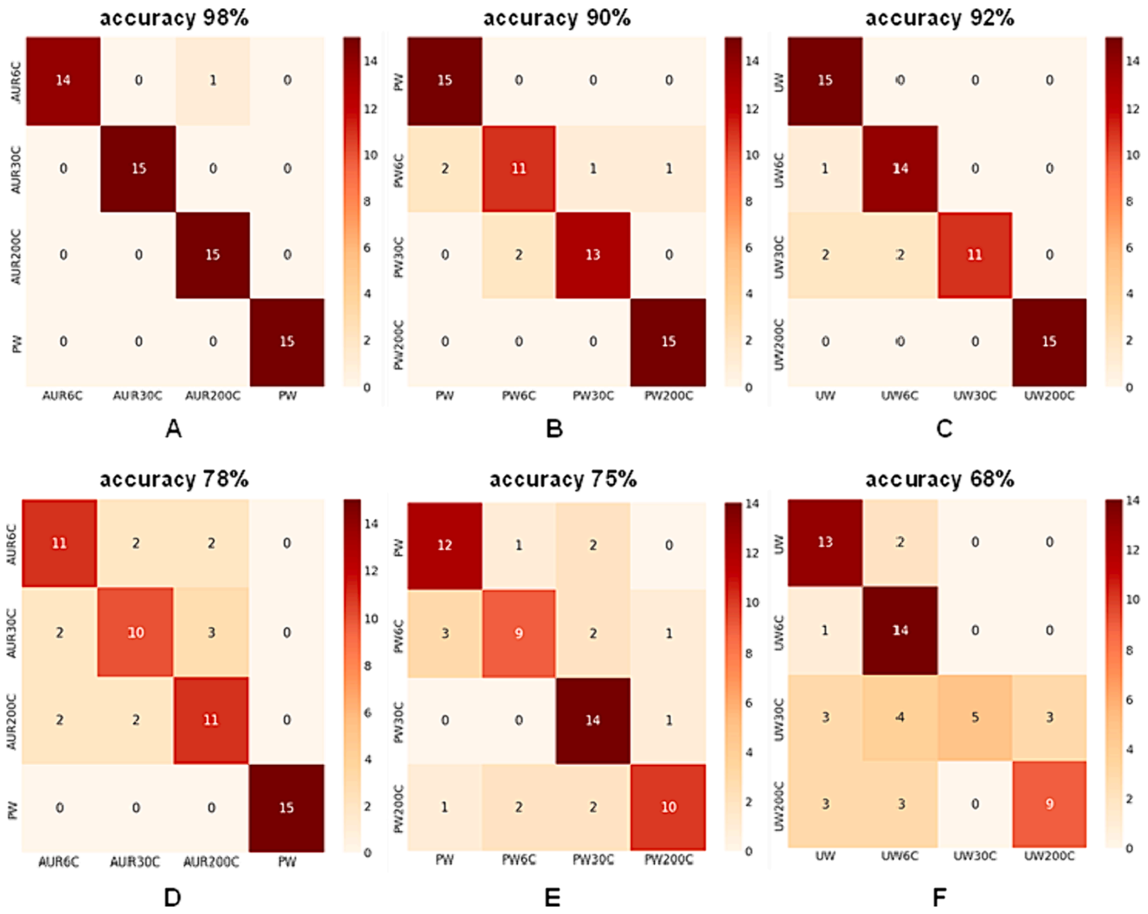

Fig. 5. Deep learning model performance for assessing the discrimination within each group using (A-B-C) unpretreated and (D-E-F) bg-pretreated data.

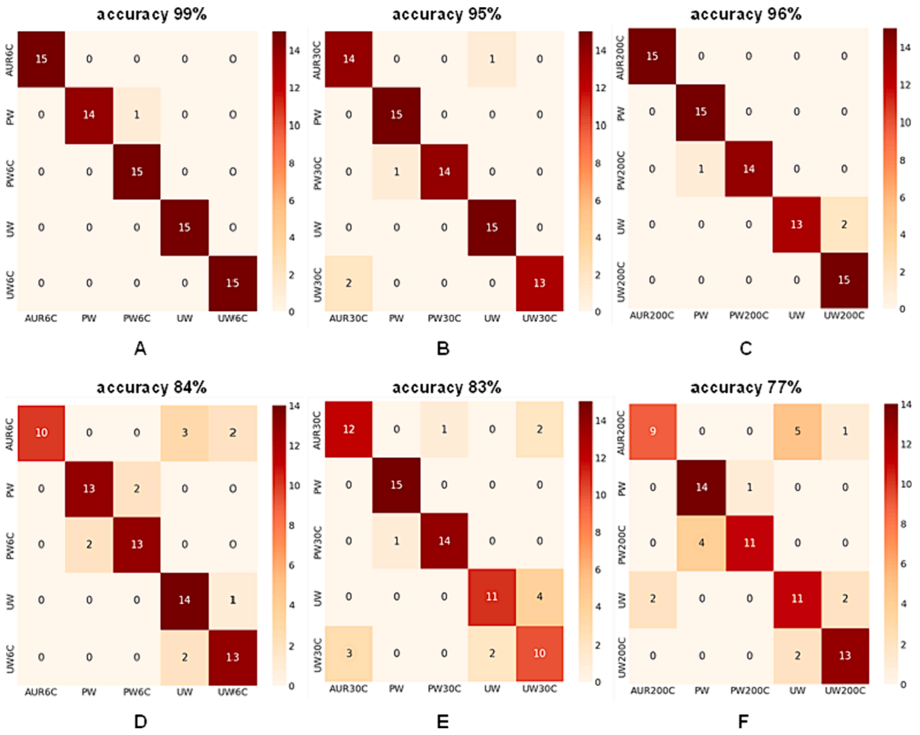

Fig. 6. Deep learning model performance for assessing the discrimination within each potentiation level using (A-B-C) unpretreated and (D-E-F) bg-pretreated data.

performance compared to the other classes. After performing a general analysis, it is clear that the AUR group has the fewest instances of incorrect classifications and that most misclassifications occur due to the great degree of resemblance between the 6C and 30C classes.

3.2.3. *Classifying within the same level of potentization with deep learning by using the GRU model*

Additionally, the performance of DL in discriminating classes within the same potentization level based on their Raman spectra was analyzed (Fig. 6). When categorizing the potentization levels, we considered five classes, including the potentized AUR, PW, and UW samples and the nonpotentized PW and UW samples as references. Analysis of the results showed that for 6C potency, accuracy values of 99 % (unpretreated) and 84 % (bg-pretreated) were obtained from the GRU model. Accuracy values of 95 % (unpretreated) and 83 % (bg-pretreated) were also found for the 30C potency. For the 200C potency, the GRU model yielded accuracy values of 96 % (unpretreated) and 77 % (bg-pretreated). Thus, the best performance of the GRU model was observed in the case of low-dilution solutions (6C).

4. Discussion

The necessity to find reliable techniques for efficient characterization of ultrahigh dilutions is well-known. In this study, we show that it is possible to use a suite of methods (TEM-EDX and Raman spectroscopy in combination with DL) for successful characterization and differentiation of highly diluted solutions that are obtained after the potentization treatment. TEM-EDX can be used to assess the composition and morphology of any colloidal solution. We show here that this technique is efficient even for highly diluted solutions, allowing us to obtain valuable information related to each level of potentization and, in this way, to discriminate them by creating an image that could be associated with each potentization level.

As a general observation, the morphology of the AUR 6C solution seems to be similar to that of usual gold nanoparticle colloidal solutions [45]; the size of gold nanoparticles depends on the nature of the raw materials used in the synthesis process. In the case of the other two potencies of AUR, 30C and 200C, their design appears to be governed by the constructal law that predicts the strategic engineering of novel architectures on the basis of a law of physics [46].

Si and O are the two elements omnipresent in the AUR 30C samples, while isolated nanoparticles containing impurities such as iron (Fe), titanium (Ti), calcium (Ca), magnesium (Mg), and aluminum (Al) are visible in the E-AUR 30C sample, whose constituents are smaller (Fig. 2 and Figs. S5-S7). These impurities either originate from the solvent used or could be formed during the potentization treatment by dissolution from the glass vials (e.g., Si or Ti). The reason that these impurities are so evident in potency 30C can be attributed to the size of the remedy's constituents, which are smaller than the constituents of the other two potencies (6C and 200C), as depicted in the histograms of Fig. 1C and G, 2C and G, and 3C and G. In addition, the filiform profile observed in the W-AUR 30C sample (Fig. 2D), the occurrence of some carbon (C)-based structures in E-AUR 30C (Fig. S7B), and the presence of gold in the two 30C potency samples (Fig. 2 inset and Figs. S5 and S8B) must be highlighted.

All these observations suggest a different organization for the 6C and 30C potencies of AUR and indicate the presence of both nanoparticles and cluster assemblies in the 30C samples. Thus, the clear nanoparticle shape of impurities and the filiform/cluster assemblies formed from small structures promote the idea that at least for AUR 30C, the observed organization is not primarily related to the nanoparticulate systems, but more to large assemblies (clusters) of small structures. Most likely, these clusters also contain ethanol and water (in E-AUR) or water (in W-AUR) molecules, while impurities, either isolated or linked to these large assemblies, appear as nanoparticles (clear round shape and different sizes). Although gold was identified in all the investigated samples, it appears scattered on the grid surface in the TEM-EDX mapping images.

The results obtained for the AUR 200C samples suggest an extended organization of AUR 200C molecules, indicating the existence of stable and organized structures over a larger area. The impurities are present as large assemblies (Fig. S10B); thus, large impurities (micrometer scale), such Si, Al, Fe and O, linked together can be seen in the TEM-EDX mapping results. The filiform profile can be also noted for the W-AUR 200C samples (Fig. 3A,3D) as well as the occurrence of some carbon (C)-based structures in E-AUR 200C (Figs. S10A and S10C), and the presence of gold in the two types of investigated 200C samples (Fig. 3 inset and Figs. S9 and S11B).

Some of these results are supported by the literature; for example, the presence of gold, even at high potencies (30C and 200C) of AUR that are beyond the Avogadro number, was also shown in the papers of Chikramane et al. [10] and Rajendran [47]. In the work of Chikramane et al., the elemental composition of TEM particles was identified by selected area electron diffraction (SAED) and confirmed by ICP–AES analysis [10]. The study of Rajendran highlights the idea that nanoparticles are found mostly on the quantum dot scale in all solutions [47]; their particle sizes are approximately similar to our data. This nanoparticulate perspective is also supported by our findings, but in addition, our results demonstrate that AUR's structure combines nanoparticles and cluster arrangements composed of smaller or larger nanostructures. These cluster arrangements are more evident for the high dilutions that are beyond the Avogadro number and are influenced by the solvent nature and by the level of potentization; the higher the potency is, the more branched and larger the formed structures are. Extension of this organization over a large area should lead to structures that are more stable and could be in accord with the constructal law of design and evolution in nature, as described by Bejan and Lorente [46].

In addition to the TEM-EDX study, we investigated whether a methodology based on Raman spectroscopy and DL is able to classify solutions that are not significantly different in structure, such as i) PW versus UW solutions, which display subtle differences since the UW used in these experiments is essentially a partially purified water used in cosmetics, and ii) PW versus AUR solutions, where the differences are due to the presence of very low concentrations of gold in the AUR samples. Moreover, the complexity and dynamics of water-based structures produce a response in the investigated Raman region (especially the OH stretching range), as demonstrated by Sun [32] and several other authors [28–31].

The results obtained for all three investigated situations (classifying all classes, classifying potencies within each group (AUR, PW, and UW) or classifying within the same level of potentization (6C, 30C and 200C) demonstrate that DL approaches can be used to easily and effectively recognize various classes. In the dataset with the baseline removed (namely, bg-pretreated), the GRU model is unable to capture the data trend in its whole. To achieve better results for bg-pretreated data, we employed quantized normalization. Furthermore, in this case, the batch-normalization technique was only applied after the final dense layer of the model. A model with two stages of recognition might be proposed as an expansion of the current study. The first model would be responsible for determining the sample type, whereas the second model would be able to separate test samples into subclasses within the sample type class. This procedure takes significantly more time, but it is believed to produce superior results. Moreover, based on the results obtained for the discrimination study involving all the 11 classes and a data augmentation approach, the use of a spectral segmentation method can be seen as a valuable strategy for increasing the model prediction accuracy.

5. Conclusion

Overall, by analyzing the results obtained from TEM-EDX and the methodology based on Raman spectroscopy and DL algorithms, we can argue that these methods can be successfully used for the characterization of ultrahigh dilutions. This suite of techniques revealed a modality that could be the basis for discriminating different remedies in accordance with the nature of the initial substances used to prepare the remedies or could allow the differentiation of samples based on their level of potentization. This approach allows the analysis of the highly diluted solutions on a far larger scale than was achievable in the past.

CRediT authorship contribution statement

Camelia Berghian-Grosan: Writing – review & editing, Writing – original draft, Supervision, Methodology, Investigation, Data curation, Conceptualization. **Sahin Isik:** Writing – review & editing, Writing – original draft, Software, Methodology. **Alin Sebastian Porav:** Writing – review & editing, Writing – original draft, Methodology, Investigation. **Ilknur Dag:** Writing – review & editing, Writing – original draft, Supervision, Methodology. **Kursad Osman Ay:** Writing – review & editing, Writing – original draft, Methodology, Investigation. **George Vithoulkas:** Writing – review & editing, Writing – original draft, Methodology, Conceptualization.

Declaration of competing interest

Camelia Berghian-Grosan and George Vithoulkas report article publishing charges was provided by International Academy of Classical Homeopathy. George Vithoulkas reports a relationship with International Academy of Classical Homeopathy that includes: board membership. If there are other authors, they declare that they have no known competing financial interests or personal relationships that could have appeared to influence the work reported in this paper.

Data availability

Data will be made available on request.

Acknowledgements

The authors would like to thank the International Academy for Classical Homeopathy (I.A.C.H.) - Alonissos (Greece) for the support provided for this research and Dr. Drosos Kourounis for his suggestions and corrections that considerably improved the quality of this manuscript. Special thanks are extended to Korres Pharmacy and Mr. George Korres (Greece, www.korres.com) for the preparation of the homeopathic solutions.

Appendix A. Supplementary material

Supplementary data to this article can be found online at https://doi.org/10.1016/j.molliq.2024.124537.

References

[1] S. Hahnemann, Organon of Medicine, 6th ed., B. Jain Publishers (P) Ltd, 2012.

[2] T.F. Allen, The encyclopedia of pure materia medica: a record of the positive effects of drugs upon the healthy human organism, Boericke & Tafel, New York, 1874.

[3] T.F. Allen, A handbook of materia medica and homoeopathic therapeutics, F.E. Boericke, Philadelphia, 1889.

[4] J.T. Kent, Lectures on Homoeopathic Materia Medica, reprint, B. Jain Publications, 2005.

[5] G. Vithoulkas, Materia Medica Viva 1-3, Homeopathic Book Publishers, London, 1995.

[6] G. Vithoulkas, Materia Medica Viva 4-13, International Academy of Classical Homeopathy, Alonissos, 1997-2021.

[7] P. Nandy, A review of basic research on homoeopathy from a physicist's point of view, Indian J. Res. Homoeopathy 9 (2015) 141, https://doi.org/10.4103/0974-7168.166372.

[8] P. Bellavite, M. Marzotto, D. Olioso, E. Moratti, A. Conforti, High-dilution effects revisited. 1. physicochemical aspects, Homeopathy 103 (2014) 4–21, https://doi.org/10.1016/j.homp.2013.08.003.

[9] P.S. Chikramane, D. Kalita, A.K. Suresh, S.G. Kane, J.R. Bellare, Why extreme dilutions reach non-zero asymptotes: a nanoparticulate hypothesis based on froth flotation, Langmuir 28 (2012) 15864–15875, https://doi.org/10.1021/la303477s.

[10] P.S. Chikramane, A.K. Suresh, J.R. Bellare, S.G. Kane, Extreme homeopathic dilutions retain starting materials: a nanoparticulate perspective, Homeopathy 99 (2010) 231–242, https://doi.org/10.1016/j.homp.2010.05.006.

[11] G.S. Anagnostatos, G. Vithoulkas, P. Garzonis, C. Tavouxoglou, A working hypothesis for homœopathic microdiluted remedies, Br. Homoeopath. J. 81 (1992) 67, https://doi.org/10.1016/S0007-0785(05)80310-2.

[12] M.O. Kokornaczyk, S. Würtenberger, S. Baumgartner, Impact of succussion on pharmaceutical preparations analyzed by means of patterns from evaporated droplets, Sci. Rep. 10 (2020) 570, https://doi.org/10.1038/s41598-019-57009-2.

[13] T.W. Randolph, E. Schiltz, D. Sederstrom, D. Steinmann, O. Mozziconacci, C. Schöneich, E. Freund, M.S. Ricci, J.F. Carpenter, C.S. Lengsfeld, Do not drop: mechanical shock in vials causes cavitation, protein aggregation, and particle formation, J. Pharm. Sci. 104 (2015) 602–611, https://doi.org/10.1002/jps.24259.

[14] A. Gerhardt, N.R. Mcgraw, D.K. Schwartz, J.S. Bee, J.F. Carpenter, T.W. Randolph, Protein aggregation and particle formation in prefilled glass syringes, J. Pharm. Sci. 103 (2014) 1601–1612, https://doi.org/10.1002/jps.23973.

[15] S. Novella, R. Roy, D. Marcus, I.R. Bell, N. Davidovitch, A. Saine, A. Debate, Homeopathy—Quackery or a key to the future of medicine? J. Altern. Complement. Med. 14 (2008) 9–15, https://doi.org/10.1089/acm.2007.0770.

[16] V. Elia, M. Niccoli, New physico-chemical properties of extremely diluted aqueous solutions, J. Therm. Anal. Calorim. 75 (2004) 815–836, https://doi.org/10.1023/B:JTAN.0000027178.11665.8f.

[17] I. Botha, A.H.A. Ross, A nuclear magnetic resonance spectroscopy comparison of 3C trituration derived and 4C trituration derived remedies, Homeopathy 97 (2008) 196–201, https://doi.org/10.1016/j.homp.2008.08.008.

[18] M. van Wassenhoven, M. Goyens, M. Henry, E. Capieaux, P. Devos, Nuclear magnetic resonance characterization of traditional homeopathically manufactured copper (Cuprum metallicum) and plant (Gelsemium sempervirens) medicines and controls, Homeopathy 106 (2017) 223–239, https://doi.org/10.1016/j.homp.2017.08.001.

[19] M. van Wassenhoven, M. Goyens, E. Capieaux, P. Devos, P. Dorfman, Nanoparticle characterisation of traditional homeopathically manufactured Cuprum metallicum and Gelsemium sempervirens medicines and controls, Homeopathy 107 (2018) 244–263, https://doi.org/10.1055/s-0038-1666864.

[20] F. Esposito, U. Wolf, S. Baumgartner, NMR relaxation time investigation of highly diluted aqueous solutions of silica-lactose, J. Mol. Liq. 337 (2021) 115975, https://doi.org/10.1016/j.molliq.2021.115975.

[21] M. van Wassenhoven, M. Goyens, M. Henry, J. Cumps, P. Devos, Verification of nuclear magnetic resonance characterization of traditional homeopathically manufactured metal (Cuprum metallicum) and plant (Gelsemium sempervirens) medicines and controls, Homeopathy 110 (2021) 042–051, https://doi.org/10.1055/s-0040-1710022.

[22] M. van Wassenhoven, M. Goyens, P. Dorfman, P. Devos, Particle characterisation of traditional homeopathically manufactured medicine cuprum metallicum and controls, Int J High Dilution Res 20 (2021) 11–28. https://doi.org/10.51910/ijhdr.v20i4.1113.

[23] M. van Wassenhoven, B. Nysten, M. Goyens, P. Dorfman, P. Devos, D. Magnin, The ion partition detected in homeopathically manufactured medicine cuprum metallicum and controls, Int. J. High Dilution Res. 21 (2022) 67–84. https://doi.org/10.51910/ijhdr.v21icf.1181.

[24] H.N. Bhargaw, M. Sharma, A.K. Srivastava, N. Nambison, M.K. Gupta, M. R. Jadhav, K.S. Gavel, P.K. Baghel, M. Ahmed, Unraveling the low-frequency triggered electromagnetic signatures in potentized homeopathic medicine, Mater. Sci. Eng. B 292 (2023) 116365, https://doi.org/10.1016/j.mseb.2023.116365.

[25] E. Davenas, F. Beauvais, J. Amara, M. Oberbaum, B. Robinzon, A. Miadonnai, A. Tedeschi, B. Pomeranz, P. Fortner, P. Belon, J. Sainte-Laudy, B. Poitevin, J. Benveniste, Human basophil degranulation triggered by very dilute antiserum against IgE, Nature 333 (1988) 816–818, https://doi.org/10.1038/333816a0.

[26] G. Vithoulkas, The controversy over the "Memory of Water", Med. Sci. Hypotheses 4 (2017) 1–6. https://doi.org/10.12659/MSH.901167.

[27] B. Bagchi, Water in biological and chemical processes: from structure and dynamics to function, Cambridge University Press, 2013.

[28] A. Nilsson, L.G.M. Pettersson, The structural origin of anomalous properties of liquid water, Nat. Commun. 6 (2015) 8998, https://doi.org/10.1038/ncomms9998.

[29] L.G.M. Pettersson, R.H. Henchman, A. Nilsson, Water-the Most Anomalous Liquid, Chem. Rev. 116 (2016) 7459–7462, https://doi.org/10.1021/acs.chemrev.6b00363.

[30] J. Liu, X. He, J.Z.H. Zhang, L.-W. Qi, Hydrogen-bond structure dynamics in bulk water: insights from *ab initio* simulations with coupled cluster theory, Chem. Sci. 9 (2018) 2065–2073, https://doi.org/10.1039/C7SC04205A.

[31] F. Perakis, L. De Marco, A. Shalit, F. Tang, Z.R. Kann, T.D. Kühne, R. Torre, M. Bonn, Y. Nagata, Vibrational spectroscopy and dynamics of water, Chem. Rev. 116 (2016) 7590–7607, https://doi.org/10.1021/acs.chemrev.5b00640.

[32] Q. Sun, The Raman OH stretching bands of liquid water, Vib. Spectrosc 51 (2009) 213–217, https://doi.org/10.1016/j.vibspec.2009.05.002.

[33] S. Guo, J. Popp, T. Bocklitz, Chemometric analysis in Raman spectroscopy from experimental design to machine learning–based modeling, Nat. Protoc. 16 (2021) 5426–5459, https://doi.org/10.1038/s41596-021-00620-3.

[34] C.M. Bishop, Neural networks for pattern recognition, Clarendon Press, Oxford, 1995.

[35] A. Gron, Hands-on machine learning with Scikit-learn, Keras, and tensorflow: concepts, tools, and techniques to build intelligent systems, 2nd ed., O'Reilly Media, 2019.

[36] J.F. Díez-Pastor, S.E. Jorge-Villar, Á. Arnaiz-González, C.I. García-Osorio, Y. Díaz-Acha, M. Campeny, J. Bosch, J.C. Melgarejo, Machine learning algorithms applied to Raman spectra for the identification of variscite originating from the mining complex of Gavà, J. Raman Spectrosc. 51 (2020) 1563–1574, https://doi.org/10.1002/jrs.5509.

[37] J. Houston, F.G. Glavin, M.G. Madden, Robust classification of high-dimensional spectroscopy data using deep learning and data synthesis, J. Chem. Inf. Model. 60 (2020) 1936–1954, https://doi.org/10.1021/acs.jcim.9b01037.

[38] F. Lussier, V. Thibault, B. Charron, G.Q. Wallace, J.-F. Masson, Deep learning and artificial intelligence methods for Raman and surface-enhanced Raman scattering, TrAC Trends Anal. Chem. 124 (2020) 115796, https://doi.org/10.1016/j.trac.2019.115796.

[39] Y. Lecun, L. Bottou, Y. Bengio, P. Haffner, Gradient-based learning applied to document recognition, Proc. IEEE 86 (1998) 2278–2324, https://doi.org/10.1109/5.726791.

[40] K. Cho, B. Van Merrienboer, C. Gulcehre, D. Bahdanau, F. Bougares, H. Schwenk, Y. Bengio, Learning Phrase Representations using RNN Encoder–Decoder for Statistical Machine Translation, in: Proceedings of the 2014 Conference on Empirical Methods in Natural Language Processing (EMNLP), Association for Computational Linguistics, Doha, Qatar, 2014: pp. 1724–1734. https://doi.org/10.3115/v1/D14-1179.

[41] M.H. Wathsala N. Jinadasa, A. C. Kahawalage, M. Halstensen, N.-O. Skeie, K.-J. Jens, Deep Learning Approach for Raman Spectroscopy, in: C. Shakher Pathak, S. Kumar (Eds.), Recent Developments in Atomic Force Microscopy and Raman Spectroscopy for Materials Characterization, IntechOpen, 2022. https://doi.org/10.5772/intechopen.99770.

[42] R. Pascanu, T. Mikolov, Y. Bengio, On the difficulty of training Recurrent Neural Networks, 2013. https://doi.org/10.48550/ARXIV.1211.5063.

[43] KORRES Homeopathic Production Unit, An Introduction to Homeopathic Pharmacopoeia and Production Guidelines, (n.d.). https://youtube/NkNe-33Q008 (accessed April 23, 2023).

[44] OriginPro, OriginLab Corporation. Create and Subtract Baseline with Peak Analyzer https://www.originlab.com/doc/Tutorials/Create-Subtract-Baseline (accessed March 12, 2024).

[45] F. Chen, Y. Wang, J. Ma, G. Yang, A biocompatible synthesis of gold nanoparticles by tris(hydroxymethyl)aminomethane, Nanoscale Res. Lett. 9 (2014) 220, https://doi.org/10.1186/1556-276X-9-220.

[46] A. Bejan, S. Lorente, The constructal law of design and evolution in nature, Phil. Trans. R. Soc. B 365 (2010) 1335–1347, https://doi.org/10.1098/rstb.2009.0302.

[47] E.S. Rajendran, Homeopathy a material science: nanoparticle characterization of Aurum metallicum 6C, 30C, 200C, 1000C, 10000C, 50000C and 100000C, Int. J. Curr. Res. 9 (2017) 48923–48927.